Journal of Materials Chemistry A

ROYAL SOCIETY OF CHEMISTRY

PAPER

Cite this: J. Mater. Chem. A, 2025, 13, 35632

Enhancing catalytic oxygen reduction *via* sulfonate and phosphate crosslinkers in redox polyelectrolyte-based O_2–glucose membraneless enzymatic biofuel cells

Agustina Köhler, [a] Sonia A. Wirth, [bc] M. Lorena Cortez, [d] Omar Azzaroni, [d] Julia Alvarez-Malmagro, [e] Francisco Prieto-Dapena, [e] Santiago E. Herrera, [af] Fernando Battaglini *[af] and Lucy L. Coria-Oriundo *[af]

The development of enzymatic biofuel cells (EBFCs) that operate under mild conditions and do not require membranes as separators is crucial for advancing low-power device technologies. The use of redox mediators for bacterial laccases represents a promising approach in these systems. In this study, a redox polyelectrolyte based on branched polyethyleneimine modified with an osmium complex (Os(im)PEI) was employed as the mediator. Os(im)PEI aggregates the nanomolar scale in the presence of species containing sulfonate or phosphate groups, depending on their concentration and ionic strength (IS). At 1 mM tripolyphosphate (TPP) under high IS, the polyelectrolyte matrix yielded particles formation (400 nm), while with 50 mM HEPES under low IS resulted in smaller particles (220 nm) along with free polyelectrolyte. These redox particles were self-assembled layer-by-layer in combination with the bacterial laccase SilA to construct a biocathode. The catalytic current density increased consistently up to the third bilayer in both systems, with the highest adsorbed mass observed in the presence of TPP. Notably, the incorporation of both species enhanced the redox polyelectrolyte's function as an enzyme mediator compared to its free form. This enhancement, linked to increased SilA adsorption, may stem from stronger surface electrostatic interactions and changes in overall wettability—attributable to the polyelectrolyte's globular conformation—or from specific interactions between phosphate groups and basic residues on laccase. Using these biocathodes along with a bioanode, O_2–glucose membraneless EBFCs were constructed under neutral pH and static conditions, achieving power densities ranging from 25 to 47 μW cm^{-2}. These values were comparable to, and in some cases exceeded, those reported in previous studies under similar operating conditions.

Received 21st July 2025
Accepted 16th September 2025

DOI: 10.1039/d5ta05877e

rsc.li/materials-a

1 Introduction

In recent years, there has been a steady increase in the demand for renewable and sustainable energy sources for power generation, driven by growing concerns over the environmental impact of fossil fuels. This shift has accelerated the transition toward cleaner energy technologies aimed at securing a more sustainable and resilient energy future.[1–4] Among power generation and storage technologies, lithium-ion batteries are currently the most widely adopted. However, their inherent rigidity and the use of potentially toxic materials pose environmental and safety risks, particularly for emerging applications such as wearable and implantable devices. Consequently, there is an urgent need for the development of flexible, biocompatible, and environmentally sustainable energy devices.[5,6]

Enzymatic biofuel cells (EBFCs) have emerged as a promising green power source that generates electricity through enzyme-catalyzed redox reactions using renewable fuels (such as biological fluids or metabolites), redox enzymes and biocompatible materials. EBFCs offer several advantages, including high energy conversion efficiency, easy recharge-

[a]Universidad de Buenos Aires, Facultad de Ciencias Exactas y Naturales, Departamento de Química Inorgánica Analítica y Química Física, C1428 Ciudad Autónoma de Buenos Aires, Argentina. E-mail: coria@qi.fcen.uba.ar; battagli@qi.fcen.uba.ar

[b]Laboratorio de Agrobiotecnología, Departamento de Fisiología, Biología Molecular y Celular, Facultad de Ciencias Exactas y Naturales, Universidad de Buenos Aires, Intendente Güiraldes 2160, Ciudad Universitaria, C1428EGA, Argentina

[c]Instituto de Biodiversidad y Biología Experimental y Aplicada (IBBEA), CONICET – Universidad de Buenos Aires, C1428 Ciudad Autónoma de Buenos Aires, Argentina

[d]Instituto de Investigaciones Fisicoquímicas Teóricas y Aplicadas (INIFTA), (UNLP, CONICET), Sucursal 4, Casilla de Correo 16, 1900 La Plata, Argentina

[e]Departamento de Química Física, Universidad de Sevilla, C/Profesor García González n 2, 41012 Seville, Spain

[f]Instituto de Química de los Materiales, Ambiente y Energía (INQUIMAE), CONICET – Universidad de Buenos Aires, C1428 Ciudad Autónoma de Buenos Aires, Argentina

ability, environmental friendliness, intrinsic safety and the potential for miniaturization. Additionally, they can operate effectively within the physiological pH and body temperature, making them well-suited for powering on-body electronic devices such as wearable or implantable biomedical devices.[1,5,7–9]

Among EBFCs, those based on glucose oxidation and oxygen reduction reactions, are especially attractive due to the abundant availability of these reactants in biological fluids.[10,11] Recent advances in EBFCs design have focused on enhancing performance enzyme immobilization—emphasizing stability, control and surface coverage—, advanced redox mediation strategies, and increased cathodic oxygen reduction current.[3,12,13] Nevertheless, the oxygen reduction reaction remains a limiting factor due to its slow kinetics, low solubility, mass transfer issues, and the high bond dissociation energy of O_2.[6,14] Laccases (EC 1.10.3.2) are frequently employed as cathodic enzymes effectively reducing oxygen to water without generating toxic intermediates.[5,15–17] In particular, bacterial laccases are gaining importance due their stability, halide tolerance, and enzymatic activity at neutral pH.[18–20]

Direct electron transfer between the active site of the enzyme and the electrode surface remains challenging due to spatial separation and enzyme orientation, thus mediated electron transfer—using species that act as artificial substrate—emerges as an excellent strategy to enhance current densities.[5,15,17,21] Redox mediators must have fast electron transfer capabilities, adopt a nanostructured conformation, possess high surface charge density, remain stable in their oxidation states, and have a formal potential close to that of the enzyme.[5,15,22,23] The usual redox mediators employed in the construction of biocathode with laccases include acetosyringone, promazine, 2,2′-azinobis(3-ethylbenzothiazoline-6-sulfonic acid) (ABTS) and its derivatives, and redox polyelectrolytes with osmium or copper complexes and quinones as active groups.[3,24–26] Redox polyelectrolytes can exhibit different characteristics in terms of electron transfer and reaction kinetics, depending on their structure, charge, the number of redox moieties, and reduction potential. Those based on osmium complexes have been extensively studied for bioelectrode construction, due to their tunable redox potential, reversible redox behavior, pH independence, and high stability.[27–30] To fulfill the additional requirements of the device, such as fast electron transfer, surface stability, and enzyme retention, a suitable immobilization approach should be employed. The primary objective is to create a gel-like structure that facilitates close interaction between the redox polyelectrolyte and the enzyme while maintaining segmental mobility to enable electron transport through the film.[24,27]

The conformation of the backbone chains of a polyelectrolyte is strongly influenced by medium pH, ionic strength and the type of ions in the solution, enabling them to generate complex structures with other macromolecules, such as enzymes. Particularly, the most common polyelectrolyte complexes are formed spontaneously through a self-assembly process and are primarily driven by entropy change and electrostatic forces, but also by other interactions such as hydrogen bonding or van der Waals.[31–42] It has been previously reported that redox polyamines (linear or branched) can undergo conformational changes in the presence of monovalent ions (*e.g.*, bromide, chloride, fluoride, *etc.*). These ions act as co-ions forming ionic pairing and altering the hydrophobicity of the polyelectrolyte. Also, the presence of multivalent ions (phosphate or sulfate ions) has significant effects on polyelectrolytes inducing aggregation, altering rheological properties, modulating adsorption on surfaces, and influencing the adsorption of other macromolecules onto the polyelectrolyte, including positively charged macromolecules.[23,27–29] Organic molecules containing phosphate groups have been evaluated with different macromolecules including those with amine groups.[43,44] Conversely, for molecules with sulfonate group the most widely studied is polystyrenesulfonate (PSS), since other species have primarily been used as pH regulators.[45] In both cases, sulfonate and phosphate species can interact with amino groups, specifically with certain amino acids such as lysine and arginine, through electrostatic and hydrogen bonding interactions, thereby enhancing their interaction with an enzyme.[43,46–49] Additionally, the structure of the organic part of the molecule and the presence of other functional groups can play a significant role in interactions with a polyamine or enzyme.

In this study, we present results using 4-(2-hydroxyethyl)-1-piperazineethanesulfonic acid (HEPES), isethionic acid, tripolyphosphate, and sodium dodecyl phosphate (Fig. 1) as crosslinking agents to enhance the interaction between a branched polyethyleneimine with pendant osmium complexes and a bacterial laccase (SilA) in gel-like layer-by-layer self-assembled structures immobilized on the electrode surface. We investigated the effect of crosslinker type, concentration, and ionic strength during the assembly of the redox polyelectrolyte–laccase system on several parameters that characterize biofuel cell performance, such as adsorbed material, electron hopping efficiency, and oxygen reduction catalysis.

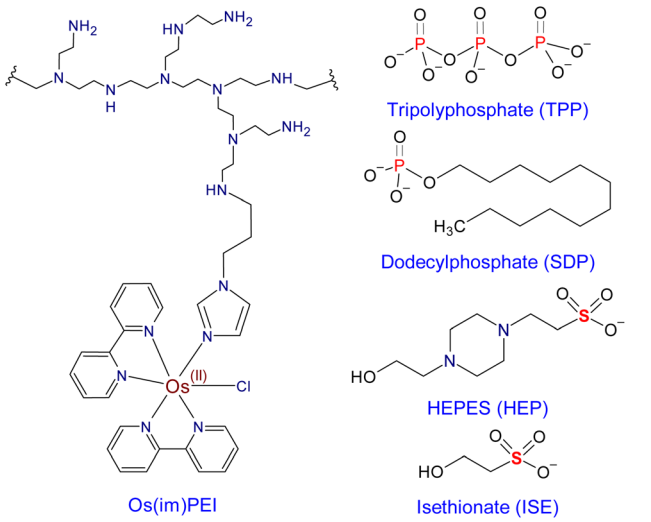

Fig. 1 Chemical structures of osmium-based redox polyelectrolyte (Os(im)PEI) and species with phosphate or sulfonate groups studied in this work.

Additionally, the biocathode was evaluated under neutral and static conditions, together with a pyrroloquinoline-dependent glucose dehydrogenase (PQQ-GDH)-based bioanode in a membraneless enzymatic fuel cell saturated with glucose and oxygen.

2 Experimental

2.1 Reagents and materials

$OsCl_6(NH_4)_2$, imidazole, 2-(2-bromoethyl)-1,3-dioxolane, tetrabutylammonium bromide, ammonium hexafluorophosphate, 4,4′-dimethoxy-2,2′-bipyridine (dmobpy), and branched polyethyleneimine (PEI, cat #408727) were procured from Sigma-Aldrich; 2,2′-bipyridine (bpy) was provided by Fluka. All other reagents were of analytical grade. Ultrapure water (18 Mohm) was used to prepare the solutions.

2.2 Redox polyelectrolyte synthesis

The complexes OsL_2Cl_2, where L is a bipyridinic ligand, bpy or dmobpy, were synthesized following the procedure reported by Buckingham *et al.*[50] The *N*-(2-(2-ethyl)-1,3-dioxolane imidazole) (ImDiox) ligand was synthetized by reaction between purified imidazole and 2-(2-bromoethyl)-1,3-dioxolane following the procedure described by Mao *et al.*[51] The complexes $OsL_2Cl(imDiox)^+$ were synthetized as reported by Kober *et al.*[52] for OsL_2ClX^+ complexes. $OsL_2Cl(imCHO)PF_6$ complexes were prepared by hydrolysis to form imCHO (1*H*-imidazole-1-propanal) and subsequent precipitation. The redox polyelectrolytes Os(im)PEI and Os(OMe)PAA were synthesized as previously reported using branched polyethyleneimine (PEI) or polyallylamine (PAA), and $OsL_2Cl(imCHO)PF_6$ with bpy or dmobpy ligand, respectively.[27] The unreacted osmium complex was removed by dialysis using a 3 kDa cut-off membrane against acidified water at pH 3.0 with HCl. The content of the osmium complex and the osmium : amine ratio was determined by UV-vis spectrophotometry and ^{1}H-RMN, respectively. The redox polyelectrolyte studied for biocathode construction, Os(im)PEI, has an osmium : amine ratio of 1 : 50.

2.3 Production and purification of recombinant SilA from *Streptomyces ipomoeae*

Recombinant laccase SilA from *Streptomyces ipomoeae* was produced in bacterial *Escherichia coli* and purified by Ni–NTA (nickel–nitrilotriacetic acid) affinity chromatography as previously described.[23] The purified activity of SilA was determined by 2,6-dimethylphenol (DMP) oxidation (4570 UE L^{-1}, pH 8, 25 °C) and total protein concentration (16.4 mg mL^{-1}) was measured following the Bradford method, using bovine serum albumin (BSA) as protein standard.[53]

2.4 Graphite electrode modification

A screen-printed three-electrode system with a graphite working electrode was used.[54] For layer-by-layer assemblies, Os(im)PEI was dissolved at a final osmium concentration of 33 μM in the matrices listed in Table 1, while 0.5 mg mL^{-1} SilA enzyme was dissolved in water pH 7. Electrodes were modified following the procedure previously described by Coria-Oriundo *et al.*[27] The working electrode was sequentially exposed to 15 μL of redox polyelectrolyte and SilA solution and left for 20 minutes in a closed container with controlled humidity (92% RH). In between steps, the electrodes were washed with ultrapure water, and finally, they were dried with a flux of nitrogen and used for electrochemical experiments.

Table 1 Composition and nomenclature of matrices used with the redox polyelectrolyte[a]

Solution composition	Nomenclature[b]
NaCl	@*Y*
Tripolyphosphate + NaCl	@TPP*X*,*Y*
Sodium dodecylphosphate + NaCl	@SDP*X*,*Y*
HEPES + NaCl	@HEP*X*,*Y*
Isethionic acid + NaCl	@ISE*X*,*Y*

[a] All solutions at pH = 7.0. [b] *X* represents the concentration in mM of the phosphate or sulphonate groups and *Y* indicates NaCl concentration: 0.1 (LIS: low ionic strength) or 1 M (HIS: high ionic strength).

2.5 Electrochemical experiments

Cyclic voltammetry measurements were carried out in a buffer solution containing 50 mM HEPES + 100 mM NaCl at pH 7.0 saturated with O_2 or N_2, using a Gamry potentiostat (Gamry Interface 1000E, Gamry Instruments). For the enzymatic biofuel cell evaluation, carbon clothes (Morgan Specialty Graphite, National Electric Carbon Products, Greenville, South Carolina, USA) electrodes were used, previously activated with a 1 : 1 isopropanol/water solution and washed with MilliQ water. The biocathode for the enzymatic biofuel cells were prepared using carbon cloth electrode modified following the same procedure for graphite electrodes. Moreover, bioanode was prepared using carbon cloth electrodes modified with glucose dehydrogenase (PQQ-GDH) and Os(OMe)PAA adapting the procedure described by Coria-Oriundo *et al.*[28] Here we use a mixture with final concentrations of 0.57 mM in osmium centers from Os(OMe)PAA, 10 mM phosphate buffer pH 7 and 2 mg mL^{-1} PQQ-GDH. The modified carbon cloth electrodes were immersed in 100 mM glucose in a 50 mM HEPES + 100 mM NaCl solution saturated with O_2. Scan polarization at 2 mV s^{-1} was used to obtain polarization and power curves by monitoring the current as a function of potential (from the open circuit potential to 0 mV) as previously described.[27]

2.6 Dynamic light scattering (DLS) measurements

The hydrodynamic diameter of the colloids was determined by DLS employing a Zetasizer Nano ZS (ZEN3600, Malvern, UK) configured in the backscattered detection optic arrangement, that is the detector at 173° of the incident light beam, a 633 nm He–Ne laser and a temperature of 25 °C.

2.7 Infrared spectroscopy

Attenuated Total Reflectance-Fourier Transform Infrared (ATR-FTIR) spectra were obtained with a resolution of 4 cm^{-1} using

a NICOLET 6700 spectrophotometer endowed with an MCT-A detector and a VeeMax™-II accessory from PIKE Technologies for reflectance measurements. A silicon prism beveled at 60° was used as an IR window. The surface silicon prism exposed was modified with redox polyelectrolyte or SilA aqueous solutions for 20 minutes, between incubation solutions the prism was washed with MilliQ water and exposed to 100 mM NaCl aqueous solution. After each layer deposit, 500 reflectance spectra were collected with *p* and *s* polarized light (polarized in the reflection plane and in the normal to the reflection plane, respectively). In each case, the spectra of the first two bilayers were recorded. The final absorbance spectrum is represented as logarithmic (R_0/R) where R_0 and R are the reflectance spectrum of the previous redox polyelectrolyte layer and enzyme layer, respectively in the same working conditions.

2.8 Quartz crystal microbalance measurements (QCM-D)

The QCM-D experiments were performed using a Q-Sense instrument (QCM-D, Q-Sense E1, Sweden) equipped with Q-Sense Flow Module (QFM 401) following the procedure previously reported.[27] For all measurements, QSX 301 gold sensors were used. Samples were perfused using a peristatic microflow system (ISMATEC, ISM 596 Glattbrugg, Switzerland). Gold sensors were activated with O_3 and UV for 15 minutes immediately before use. All experiments were performed at a flow rate of 50 μL min^{-1} at 25 °C. The redox polyelectrolyte and SilA solutions were passed for 4 minutes, then the flow was stopped, and each solution was left in contact with the gold sensor for 20 minutes. Then, the solution was removed by fluxing MilliQ water until signal stabilization was achieved.

2.9 Atomic force microscopy (AFM)

Atomic force microscopy was conducted using an Agilent 5500 atomic force/scanning probe microscope. Tapping mode measurements were carried out using insulating PointProbe Plus PPP-NLC tips (<10 nm tip radius, a force constant of 48 N m^{-1}, a resonance frequency of 190 kHz). The topography of multilayer redox polyelectrolyte/SilA was studied over a template-stripped (TS) gold substrate with a 0.6 nm root mean square roughness prepared following the method of Weiss *et al.*[55,56] To determine the mean film thickness, a film area of 1 μm × 1 μm was gently removed by means of a soft cantilever in contact mode with a typical setpoint force of 9 V. Then, two-dimension height distribution was extracted from the AFM image, ensuring equal exposure of the substrate (etched area) and the film (non-modified area). The mean film thickness was then calculated by measuring the distance between the peaks representing the surface and the film. The average roughness parameter was determined by analyzing a 1 μm straight line across a representative AFM image of the surface. All images were analyzed using Gwyddion V2-49 (**http://gwyddion.net/**).

3 Results and discussion

With the aim of optimizing the performance of a biocathode for an O_2–glucose EBFC, we sequentially adsorbed a redox polyelectrolyte, Os(im)PEI (Fig. 1) and SilA recombinant laccase onto a graphite electrode using the layer-by-layer (LbL) self-assembly method. This method creates a macromolecular multilayer film with the enzyme immobilized on the electrode surface. In this EBFC, chemical energy is obtained through the reduction of oxygen and oxidation of glucose. The oxygen reduction process at the biocathode is catalyzed by laccase, with the redox polyelectrolyte acting as the mediator, with a formal potential of 0.15 V *vs.* Ag/AgCl and an osmium : amine ratio of 1 : 50.

3.1 Crosslinking study of Os(im)PEI polyelectrolyte

First, we explored the conformational changes of the redox polyelectrolyte when exposed to different species containing phosphate or sulfonate groups (Fig. 1), as well as at varying ionic strengths (see Table 1). Dynamic light scattering experiments with 33 μM Os(im)PEI in NaCl solutions, at concentration of 0.1 M (@LIS) or 1 M (@HIS), showed the formation of small colloidal particles (Table 2), associated to conformation changes between extended chains and random coils due to the ability of chloride ions to modulate the hydrophobicity of polyamines, as previously reported.[41,57–60]

Numerous studies over the past years have reported that phosphate ions serve as cross-linking agents for amino groups, forming crosslinked particles through electrostatic and hydrogen bonding interactions.[29,43,61–65] These studies examined phosphate concentrations ranging from 1 mM to 10 mM and varying ionic strengths, with lower concentration yielding the higher current densities. The effect of ionic strength (IS) varied depending on the specific polyamine and the species involving in the self-assembly process.[27,28] For similar redox polyelectrolytes, 1 mM phosphate was optimal for crosslinking, forming particles with diameters between 500 and 700 nm.

Based on this, we studied the effect of tripolyphosphate (TPP) solutions containing 1 mM phosphate at low (@TPP1,LIS) or high (@TPP1,HIS) IS (matrices for Os(im)PEI). In both conditions, colloidal particle formation was observed, with no free polyelectrolyte detected, indicating the complete integration of the redox polyelectrolyte into the particles. TPP promotes

Table 2 Os(im)PEI solutions studied by Dynamic Light Scattering (DLS)

Matrix	Diameter (nm)	PDI
@LIS	33 ± 4	0.4
@HIS	70 ± 40	0.8
@TPP1,LIS	600 ± 100	0.6
@TPP1,HIS	400 ± 50	1.0
@SDP1,LIS	600 ± 100	0.5
	150 ± 20	
@SDP1,HIS[a]	740 ± 90	0.5
@HEP50,LIS	34 ± 6	0.9
	220 ± 30	
@HEP50,HIS[a]	30 ± 10	0.6
@ISE50,LIS	140 ± 20	0.4
@ISE50,HIS	150 ± 20	1.0

[a] Particles larger than 2 μm and solid precipitation are observed.

the formation of large colloidal particles (400 to 600 nm) with a unimodal size distribution (see Table 2). TPP has been widely used as a crosslinking agent with chitosan and linear polyethyleneimine, where its degree of ionization plays a pivotal role in determining its crosslinking efficacy.[66–70] Increasing IS results in smaller colloidal particles due to weakened electrostatic interactions caused by charge screening. Higher TPP concentrations were also evaluated (see Table S1), resulting in smaller particles, as more phosphate groups interacted with amine groups; therefore IS had a lesser effect on particle size.

Next, dodecylphosphate (SDP) was compared with TPP to investigate the impact of altering the hydrophobicity of the crosslinker. While both SDP and TPP crosslinkers induced the formation of colloidal particles, a bimodal size distribution was observed for the Os(im)PEI@SDP systems at low IS (@SDP1,LIS), and larger particles precipitated under high IS condition (@SDP1,HIS). This result is in line with the Derjaguin, Landau, Verwey, and Overbeek (DLVO) theory since SDP enhances attractive van der Waals forces between colloids that compete with repulsive electrostatic forces, leading to an increase in the size of the colloid and a tendency to aggregate more easily when increasing the IS.

Consequently, from now on, the results using matrices with phosphate groups will refer to those studied at concentrations of 1 mM in phosphate units.

Although HEPES is not typically used as a crosslinker, previous studies have reported interactions between its sulfonate and amine groups under different pH and IS conditions, including electrostatic forces and ionic or neutral hydrogen bonding. Notably, interactions between phosphate and amino groups are stronger than those between sulfonate and amino groups since phosphate are multivalent ions.[71,72] As a result, higher concentrations are required to produce colloidal particles for species with sulfonate groups compared to those with phosphate groups.

The addition of 10 mM HEPES to Os(im)PEI solution at low IS does not result in any significant differences (see Table S1) owing to the inherent conformational changes of the polyelectrolyte, while at 50 mM larger particles begin to appear (220 nm, Table 1). These behaviors demonstrate that the capabilities of these crosslinkers differ, and higher concentrations of sulfonate are necessary to achieve similar results compared to phosphate groups. With the increase in IS, large particles predominantly form and precipitate, leaving free polyelectrolyte in solution. Furthermore, based on dissociation equilibrium, HEPES at pH 7.0 is a neutral molecule containing sulfonate, hydroxyl, and quaternary amine groups (see Fig. 1). Each of these groups can contribute to different interactions and will be influenced by variations in ionic strength.

To evaluate the effect of HEPES structure and the role of the heterocycle and quaternary amine, isethionic acid (ISE) was studied as a sulfonate-based crosslinker. At low concentrations (10 mM), the effect of ISE is similar to HEPES: free polyelectrolyte at low IS and bimodal distribution of particles at high IS. At 50 mM ISE, no free polyelectrolyte or solid precipitate is detected at either low or high IS, and the system exhibits an unimodal particle size distribution centered at 140–150 nm. Considering the above, there are differences between HEPES and ISE due to their spatial arrangement and the presence/absence of the heterocycle. HEPES generates larger particles, whereas ISE results in no free polyelectrolyte at high concentration.

Therefore, in the following analyses, matrices containing 50 mM in sulfonate groups are presented.

3.2 Electrodes modification for catalytic O_2 reduction

Os(im)PEI was designed to have a formal potential between 0.1 and 0.2 V *vs.* Ag/AgCl, corresponding to the redox potential of bacterial laccases from *S. ipomoeae*.[73] The osmium complex $Os(bpy)_2Cl_2$ exhibits a formal potential of 0 V *vs.* Ag/AgCl.[50,52] However, when a chloride anion is substituted by imidazole acetaldehyde (imCHO), a metal–ligand charge transfer occurs, leading to an increase in the formal potential. This ligand was chosen to raise the redox potential to 0.15 V and to allow covalent bonding with the amine groups of PEI.[74,75] Os(im)PEI colloidal particles, formed by the addition of sulfonate or phosphate species, were utilized to modify graphite electrodes, creating a film on which laccase SilA was assembled.

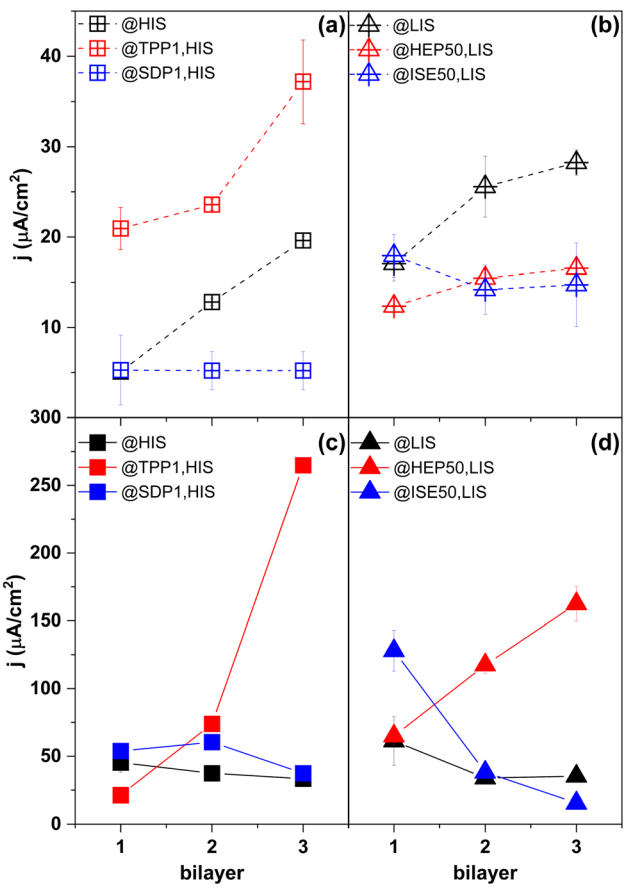

Fig. 2 Peak current densities of cyclic voltammograms after deposition of each bilayer (Os(im)PEI@*X*/SilA@H_2O), where *X* is a matrix listed in Table 1, in a solution saturated with (a and b) N_2 or (c and d) O_2. Scan rate: 10 mV s^{-1}. Buffer: 50 mM HEPES + 0.1 M NaCl, pH 7.0.

The current response of the LbL assemblies, using NaCl solutions (@LIS or @HIS for 0.1 M or 1 M concentration, respectively) as the Os(im)PEI matrix, is shown in Fig. 2a and b (black lines). In both cases, the non-catalytic response increases with each additional bilayer, although it is lower at higher IS. This reduction in response may be attributed to the weakening of the interaction between the polyelectrolyte and the electrode surface. The halide effect has been previously reported for polyamines, as the coiled conformation adopted by the redox polyelectrolyte due to ion pairing enhances its adsorption, however, adsorption decreases at higher concentrations. Also, in the presence of O_2 a significant decrease in current density with each bilayer deposited is observed (black lines, Fig. 2c and d). As the catalytic and non-catalytic current densities ratio (j_c/j_0) increases, the ability of the redox polyelectrolyte to act as a redox mediator for laccase in the constructed system is enhanced. For both systems using NaCl as matrix, j_c/j_0 tends to 1 as the number of bilayers increases, demonstrating that when the assembly is formed by the free polyelectrolyte and the enzyme, the efficiency of electronic transfer between redox sites decreases.

By using TPP 1 mM an increase in non-catalytic current density up to the third bilayer is observed, reaching 37 and 77 μA cm^{-2} for high and low IS, respectively (Fig. 2a and S1a). These values represent 1.9 and 2.5 times those obtained in the absence of TPP. The higher current density at elevated IS could be associated with the enhancement of hydrogen bonding interactions between phosphate groups of TPP and amine groups of Os(im)PEI, due to charge screening. This type of effect due to ionic strength has been previously reported in the analysis of systems containing phosphate ions and polyamines both redox and non-redox active.[27,28,43,63] In our systems, the non-catalytic current density is related to the osmium centers present in the redox polyelectrolyte adsorbed in the electrode surface. Larger particles formed with crosslinkers of high charge density, such as TPP, promote increased redox polyelectrolyte adsorption, resulting in high non-catalytic current density.

Although colloidal particles (150 and 600 nm hydrodynamic diameter, Table S1) are formed due to the presence of 1 mM SDP at low IS, which should result in a higher amount of polyelectrolyte adsorbed, no increase in j_0 is observed (Fig. S1a). This could be attributed to the internal structure of each particle, wherein the osmium centers may be rendered incapable of electron hopping. At high IS, the response is even lower than in the absence of SDP (Fig. 2a, blue line), indicating poor adsorption of Os(im)PEI. Considering that larger particles are formed with embedded redox polyelectrolyte, these particles could be easily removed during washing steps.

For HEPES matrices at 50 mM, an increasing linear trend is observed, however lower j_0 values were obtained compared to systems without a crosslinker, regardless of the IS (Fig. 2b and S1a). Based on DLS measurement for @HEP50,LIS matrix, free polyelectrolyte and a portion of the particles are being adsorbed reaching 18 μA cm^{-2} for the third bilayer. However, there is no improvement compared to the free polyelectrolyte. At high IS a lower and constant current density is observed, indicating that these conditions are not appropriate (Fig. S1a). This results in a lower and constant current density, probably due to the presence of larger particles. The responses obtained for ISE did not show a defined trend but were similar in value than those for HEPES at any IS level (Fig. 2b and S1a).

In addition to examining the effect of the crosslinkers on the redox polyelectrolyte, this study also investigates how the formation of different Os(im)PEI films influence SilA laccase adsorption, thereby affecting the catalytic O_2 reaction.

The catalytic response in the presence of TPP is significantly higher compared to SDP and the matrices in the absence of a crosslinker (Fig. 2c). The measure current density increases with the number of bilayers, reaching up 265 and 319 μA cm^{-2} maximum values for the third bilayer at high and low IS, respectively. This result shows that the adsorbed particles allow for the efficient adsorption of laccase without observable polyelectrolyte loss (Fig. 3a). Several factors may contribute to the enhanced adsorption of SilA compared to the free polyelectrolyte. First, the greater amount of polyelectrolyte adsorbed onto the surface induces more significant changes in surface electrostatic charge. Second, conformational rearrangements (globular *vs.* linear) may alter the hydrophilic/hydrophobic balance, further influencing enzyme interaction.[76] Third, the phosphate groups present on the particles can interact with basic amino acid residues of laccase—such as arginine and lysine—a well-established phenomenon.[43,48,49] The relative contribution and interplay of these mechanisms require further investigation.

Although j_0 nearly doubled with TPP compared to matrices without crosslinker, j_c increased by eight to nine times. Despite the catalytic response being higher at low IS, a greater $j_c/j_0 = 7$

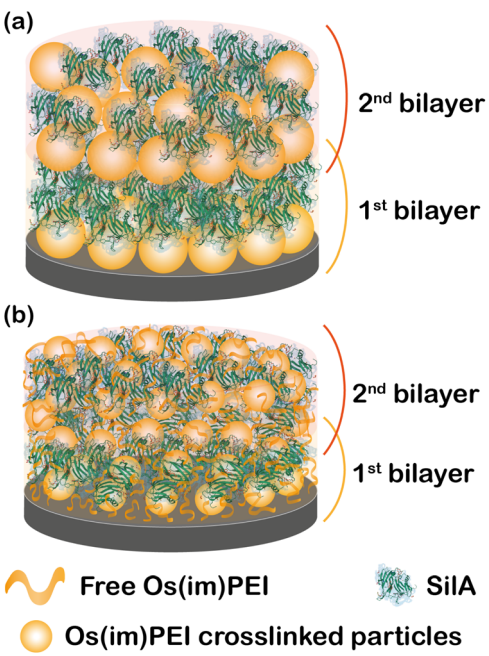

Fig. 3 Description of modified graphite electrode with LbL assemblies using Os(im)PEI in (a) @TPP1,HIS or (b) @HEP50,LIS matrix and SilA laccase.

ratio is obtained at high ionic strength. This finding suggests that particles formed at high IS enhance enzyme adsorption or improve the connectivity between redox centers.

While the values achieved with SDP are higher compared to those without crosslinker (@HIS), they are much lower than those obtained with TPP. Additionally, given that non-catalytic values are very low, this results in higher j_c/j_0 ratios. This suggests that, despite the adsorption of only a small amount of redox polyelectrolyte, the formation of these colloidal particles enhances the adsorption of the enzyme and electron transfer. This could be associated with the fact that the polyelectrolyte film becomes less hydrated, thereby, enhancing enzyme connectivity with the polyelectrolyte matrix and with the electrode surface.[76] However, for the intended application, both high catalytic currents and high j_c/j_0 ratios are required.

Regarding sulfonate species, colloidal particle formation was observed at a sulfonate concentration of 50 mM for both HEPES and ISE crosslinkers. From the HEPES matrices, free polyelectrolyte could also be adsorbed onto the graphite surface (Fig. 3b). Despite the fact that the j_0 response for @HEP50,LIS was lower compared to the matrix without the crosslinker, the maximum catalytic current density achieved was five times higher, reaching a value of 162 μA cm^{-2} (Fig. 2d). In the case of @HEP50,HIS matrix (Fig. S1a), the formation of the self-assembled system does not seem to be fully utilized, as the redox polyelectrolyte is largely washed away. The significant increase in catalytic current density with @HEP50,LIS matrix demonstrates that the formed particles not only enhance the enzyme adsorption. This improvement may result from two key factors: (i) the adoption of a new globular conformation by the redox polyelectrolyte, which alters its electrostatic properties and overall wettability,[76] and (ii) a specific interaction between the sulfonate groups of the redox polyelectrolyte and the guanidinium groups founds in the arginine residues of the SilA laccase.[46,47]

With the matrix containing ISE at low ionic strength, the highest catalytic current value was observed only for the first bilayer, after which it drastically decreased, even reaching values lower than those obtained in the absence of crosslinker (@LIS). In this case, the experimental evidence shows that the redox polyelectrolyte is washed out during successive adsorption steps, a behavior that requires further investigation.

The ionic crosslinkers that generated the highest catalytic current densities as well as the most favorable j_c/j_0 ratios were TPP and HEPES. The cyclic voltammetries from the catalytic and non-catalytic current densities obtained for the third bilayer are shown in Fig. 4. As shown, in the absence of oxygen, the voltammogram displays the characteristic profile of the surface-adsorbed osmium redox couple. In contrast, in the presence of oxygen, the voltametric response reflects catalytic reduction process mediated by osmium complexes, exhibiting minimal hysteresis. Even though higher catalytic current densities are achieved with the @TPP1,HIS matrix compared to @HEP50,LIS, the j_c/j_0 ratio with HEP increases by 30% (9.5 for HEP *vs.* 7.2 for TPP). This result suggests that the amount of adsorbed enzyme increases, or that the connectivity between the redox centers is optimized.

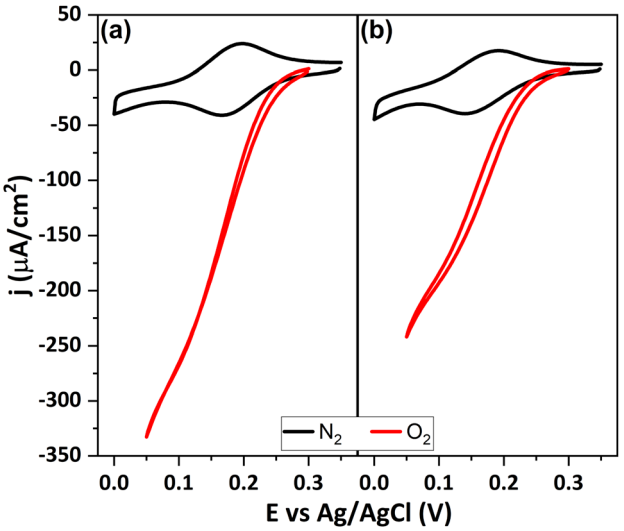

Fig. 4 Cyclic voltammetries in the presence (red lines) or in the absence (black lines) of O_2 for (a) (Os(im)PEI@TPP1,HIS/SilA@$H_2O)_3$ and (b) (Os(im)PEI@HEP50,LIS/SilA@$H_2O)_3$. Scan rate: 10 mV s^{-1}.

To assess the efficiency of electron transfer in the self-assembled systems, the electron transfer between both components in solution was also studied (Fig. S2), resulting in a $j_c/j_0 \approx 4$. Based on this reference value, the assemblies incorporating sulfonate and phosphate groups, HEPES and TPP, respectively, demonstrate a notable enhancement in electron transfer. The assembly using HEPES as the polyelectrolyte matrix improves the efficiency of electron transfer in oxygen reduction by 130% compared to that obtained in solution.

3.3 Film structure

To evaluate the difference between the films formed with @TPP1,HIS, and @HEP50,LIS due to the amount of adsorbed material or the stiffness of the film, these systems were analyzed by QCM-D. The results shown in Fig. 5 demonstrate a similar trend in frequency change in both systems, with a *ca.* 35% increase in the total mass adsorbed when TPP is incorporated in the Os(im)PEI matrix, as compared to HEPES, up to the third bilayer. The stiffness of the adsorbed film affects electron transfer, since a more rigid film reduces the mobility of osmium centers, thereby decreasing their probability of interacting with the enzyme's active sites or participating in electron hopping. In particular, the system with TPP in the polyelectrolyte matrix exhibited a 170% increase in the dissipation parameter compared to the system with HEPES. This demonstrates that the presence of TPP in Os(im)PEI results in a film with higher adsorbed mass and a lower stiffness, facilitating greater mobility of both osmium centers and the biomacromolecule, allowing it to exchange electrons more efficiently with the redox centers of the polyelectrolyte, which could be associated with the high catalytic current density obtained with @TPP1,HIS.

The structural characteristics of the LbL assemblies were investigated using AFM on a 3-bilayer Os(im)PEI/SilA film adsorbed onto a TS gold substrate, with @TPP1,HIS or

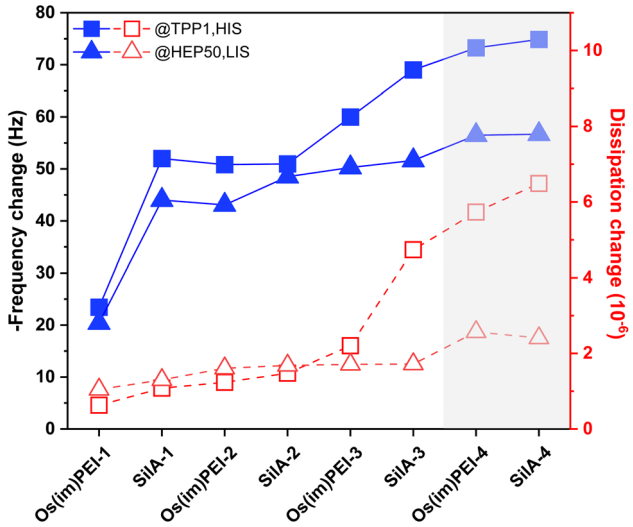

Fig. 5 QCM-D results for the assembled systems of Os(im)PEI in @TPP1,HIS or @HEP50,LIS matrix and SilA@H_2O. Blue symbols correspond to frequency changes and red to dissipation change.

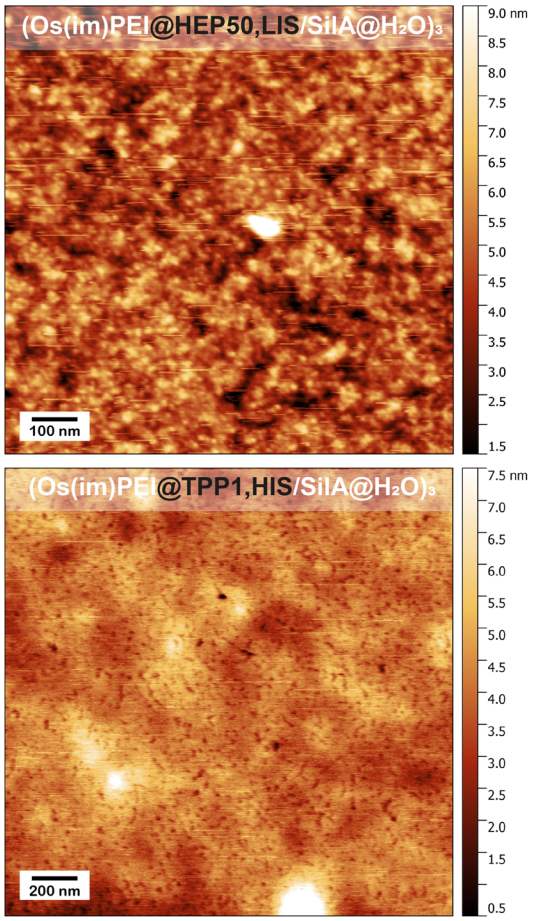

Fig. 6 AFM topography images obtained for 3-bilayer assemblies over TS gold surface using @HEP50,LIS or @TPP1,HIS as Os(im)PEI matrix.

@HEP50,LIS serving as the polyelectrolyte matrix. Fig. S3 shows the height distribution from the substrate surface to the film. Both films formed are thin, exhibiting film thicknesses of 6.6 nm and 8.3 nm for assemblies with @HEP50,LIS and @TPP1,HIS, respectively, consistent with the adsorbed mass obtained in Fig. 5. From the topographic images (Fig. 6), it can be observed that the film obtained using TPP as the polyelectrolyte matrix exhibits greater coverage, higher thickness, and lower roughness (0.6 nm) compared to the one prepared using HEPES (1.3 nm). The hydrated film thickness was estimated using QCM-D measurements and the Sauerbrey model, applying densities of 1000 kg m^{-3} for redox polyelectrolyte and 1175 kg m^{-3} for enzyme films. These values follow the same trend observed *via* AFM, with the TPP-based film being thicker (11.1 nm) than that formed with HEPES (8.3 nm). This is consistent with microgravimetry results, which shows higher adsorbed mass for TPP, while the HEPES-based film presents lower mass and higher stiffness.

Moreover, to investigate the effect of enzyme orientation upon adsorption onto these redox polyelectrolyte films, ATR-FTIR measurements were conducted. For this purpose, a silicon substrate was utilized, and the LbL assemblies were constructed following the same procedure used for the modification of graphite electrodes. The collected spectra were measured in the presence of 100 mM NaCl, simulating the conditions of electrochemical measurements, and were subsequently corrected for baseline and water signals. Each spectrum was subtracted relative to that of the preceding layers.

The ATR-FTIR spectra, presented in Fig. S4, displays the bands corresponding to amide I (1600–1700 cm^{-1}) and amide II (1490–1600 cm^{-1}), which are associated with SilA enzyme adsorbed in the second bilayer.[77] Since an aqueous solution was used to assemble both the enzyme and the redox polyelectrolyte, the water absorption band associated with H–O–H bending (1650 cm^{-1})[78] overlaps with the amide I band. Consequently, due to the attenuation of the amide I band caused by the aqueous environment, the amide II region was thoroughly analyzed to examine bands corresponding to β-sheet, α-helix, random coil, and β-turn structures. In addition, due to the penetration range of the evanescent wave generated on the surface of the silicon prism, it was possible to analyze up to the second bilayer, as the wave decreases in intensity, leading to lower absorbance values.

Dichroic relation could be determined from the integrated intensity of each tension with *p*- or *s*-polarized light (see SI section). From the spectra, it is possible to determine the ratio of the bands of the secondary structures (α/β) for both *s*- and *p*-polarized light and the angle of each with respect to the electrode surface normal (θ_α and θ_β) (Table S2).[79–81] To assess the effect of these parameters on the catalytic response of the evaluated LbL systems, the j_c/j_0 ratio obtained from these systems assembled using a crosslinker under optimal conditions was included in Table S2. Based on the results, no clear evidence can be established between these parameters and the obtained catalytic response. It should be noted that in each formed layer, the enzyme adsorbs onto different surfaces, depending on the structure adopted by the redox polyelectrolyte due to the presence of cross-linking agents. The redox

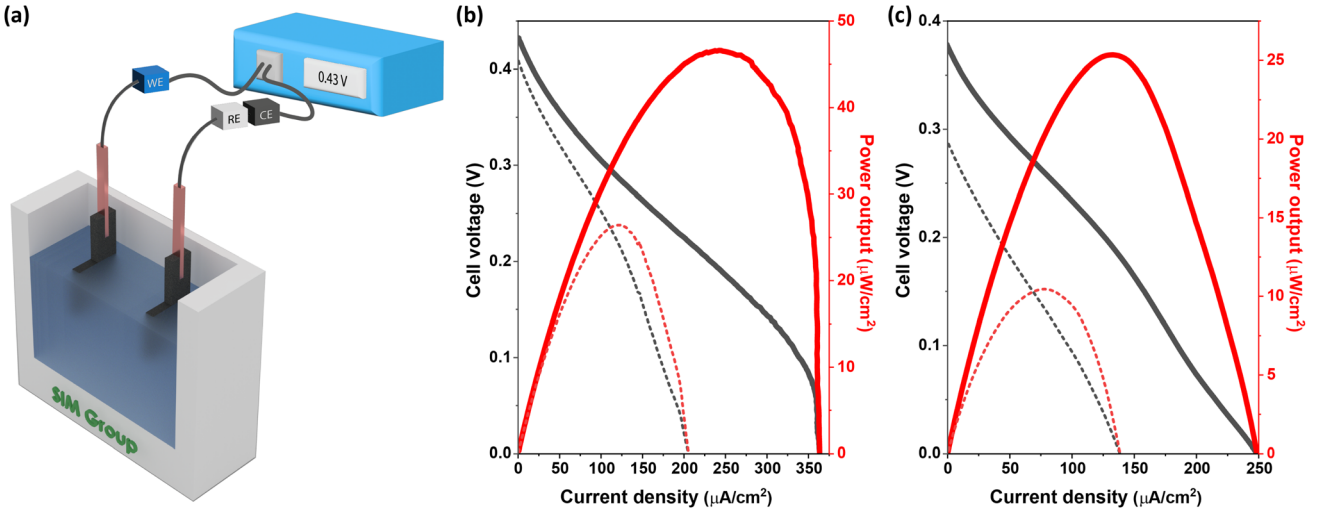

Fig. 7 (a) Scheme of measurements with a O_2–glucose membraneless EBFC, WE is connect to bioanode and CE + RE to biocathode. (b) Polarization and power curves for the EBFC using (b) (Os(im)PEI@HEP50,LIS/SilA@H_2O)$_3$ or (c) (Os(im)PEI@TPP1,HIS/SilA@H_2O)$_3$ biocathode with a bioanode, with GDH and Os(OMe)PAA immobilized, in a 0.1 M glucose in 50 mM HEPES + 0.1 M NaCl solution saturated with O_2 (pH 7). Solid and dashed lines represent the first and fifth polarization cycle, respectively.

polyelectrolyte chain, as well as the redox centers, adopt different spatial arrangements within the particles. Additionally, the organization of these particles generates surfaces with varying roughness, as observed in the AFM topographic images. Consequently, the lack of a trend in the obtained parameters from ATR-FTIR spectra could be associated with the diversity of surfaces and the wide range of orientations that the enzyme may adopt upon adsorption.[82,83] In these types of systems, due to their complexity, conducting a thorough analysis of the preferential average orientation of the enzyme remains a challenge.[21,84,85]

Overall, the presence of TPP at low concentration and high ionic strength leads to a greater amount of adsorbed material, resulting in less rigid films with increased coverage and thickness. This contributes to high current densities, reaching a maximum of 270 μA cm^{-2}. In contrast, in the presence of HEPES at higher concentrations and low ionic strength, the adsorbed mass and thickness are lower, as is the catalytic current density (162 μA cm^{-2}).

3.4 O_2–glucose membraneless enzymatic biofuel cell

Finally, the LbL systems with Os(im)PEI in @TPP1,HIS and @HEP50,LIS with SilA laccase were evaluated as biocathodes in an enzymatic biofuel cell. Here, dissolved oxygen is used as oxidant, while glucose is used as fuel. This type of EBFC works at mild conditions, (room temperature and neutral pH), does not require a membrane as a separator, and operates under static conditions. These characteristics make it suitable for use in implantable medical devices or self-powered biosensors that require low energy consumption. For glucose oxidation, a bioanode based on a similar redox polyelectrolyte with a lower formal potential was used (see Fig. S5). Additionally, since a membraneless cell is used, glucose dehydrogenase (GDH) was selected as the biocatalyst, as dissolved oxygen in solution does not compete as a co-substrate and therefore does not suppress the electrical response. This contrasts with enzymes like glucose oxidase, which are commonly used to catalyze this reaction but rely on oxygen as their natural co-substrate. Also, to assess the optimization of biocathode construction, electrolyte containing 100 mM glucose was employed in order to mitigate anodic limitations.

Fig. 7a schematically represents the assembled EBFC, consisting of a two-electrode system with modified carbon felt electrodes: bioanode and biocathode, submerged in a solution with the oxidant (oxygen-saturated) and the fuel (100 mM glucose), connected to a potentiostat.

The EBFC with Os(im)PEI@HEP50,LIS as biocathode shows an open-circuit voltage (OCV) of 0.43 V, yielding a maximum current density of 363 μA cm^{-2} and a power output of 47 μW cm^{-2} (Fig. 7b). Moreover, when the EBFC with Os(im)PEI@TPP1,HIS is used biocathode, an open-circuit voltage of 0.38 V, yielding a maximum current density of 248 μA cm^{-2} and a power output of 25 μW cm^{-2} (Fig. 7c).

Table 3 presents power output and circuit voltages obtained from recent literature, highlighting key characteristics such as the use of enzymes as catalysts at both electrodes, operation under neutral pH conditions, and the absence of membranes. These parameters facilitate a more accurate comparison with the EBFCs constructed in this study. In most of these studies, fungal laccases were employed as biocathode catalysts, as they are characterized by a higher redox potential compared to bacterial laccase. However, the latter are resistant to high halide concentration and remain active in neutral to basic media, which enhances the catalytic current response and allows their use in biological fluids.

Based on the formal potential of the redox mediators used in each bioelectrode, the theoretical cell voltage is 0.25 V. The obtained OCV is higher than the expected value, which depends

Table 3 Power output (P) and open circuit voltage (OCV) for membraneless O_2–glucose enzymatic biofuel cell employing laccases as a biocatalyst and operating at neutral pH[a]

Biocathode	Bioanode	OCV (V)	P (μW cm^{-2})	Ref.
CT/Au/PEI-Lac	CT/Ag/PEI-GOx-ferritin	0.51	98	86
Paper/FR/Shellac/rGO/Lac *A. niger*	Paper/FR/Shellac/rGO/GOx	0.39	67	87
CMEMS/PEDOT-PGAL/Lac *T. versicolor*	CMEMS/PEDOT-PGAL/GOx	0.08	0.2	88
CC/Lac *A. niger*	CC/GOx	0.48	86	89
Au/(Lac *A. bisporus*-SWCNT-(PVI-Os-dCl))$_2$/(Lac *A. bisporus*-(PVI-Os-dCl))$_2$	Au/GOx-SWCNT-(PVI-Os-dmo)$_3$/GOx-(PVI-Os-dmo)$_3$/Aga-TREH	0.58	1.2	90
CP/PTFE/SWCNT/Lac *T. versicolor*	CP/PTFE/AuNPs/C12/GOx	0.45	53	91
Graphite/AuNPs/Lac *T. hirsuta*[b]	Graphene/AuNPs/*Ct*CDH-C291Y/PVA-SbQ[b]	0.58	1.6	92
AuNT/polyimide/MUA/Lac *T. versicolor*	AuNT/polyimide/MUA/GOx	0.56	112	93
CF/(Os(im)PEI@HEP50,LIS/SilA@H_2O)$_3$	CF/Os(OMe)PAA@GDH,Pi10	0.43	47	This work
CF/(Os(im)PEI@TPP1,HIS/SilA@H_2O)$_3$	CF/Os(OMe)PAA@GDH,Pi10	0.41	26	

[a] CT: carbon thread, GOx: glucose oxidase, Lac: laccase, FR: fire retardant, rGO: reduced graphene oxide, CMEMS: carbon microelectromechanical system, PEDOT: poly(3,4-ethylene dioxythiophene), PGAL: poly(gallic acid), CC: carbon cloth, SWCNT: single walled carbon nanotube, PVI-Os-dCl: poly(*N*-vinylimidazole)-[Os(4,4′-dichloro-2,2′-bipyridine$_2$)Cl$_2$], PVI-Os-dmo: poly(*N*-vinylimidazole)-[Os(4,4′-dimethoxy-2,2′-bipyridine$_2$)Cl$_2$], Aga: agarose, TREH: trehalose, CP: carbon paper, PTFE: polytetrafluoroethylene, C12: 1-dodecanethiol, *Ct*CDH-C291Y: cellobiose dehydrogenase C291Y, PVA-SbQ: poly(vinyl alcohol)-*N*-methyl-4(4′-formylstyryl)pyridinium methosulfate acetal, AuNT: gold nanotip, MUA: 11-mercaptoundecanoic acid, CF: carbon felt. [b] EBFC operating at pH 6.5.

on the equilibrium potential, in turn influenced by the concentration of osmium centers present due to the polyelectrolyte film formed on the electrode.[84,94] The OCV and power values obtained for the EBFCs constructed in this study were found to be comparable to, and even higher than those reported in the literature. The OCV values obtained can be considered suitable for bioelectronic applications powering sub-1 V devices such as organic electrochemical transistor and graphene-based electrolyte-gated transistors.[95,96] It is worth noting that most previous studies employed carbon-based nanostructured materials, which are characterized by increasing the modified surface area or incorporating metallic nanoparticles to enhance electron transfer. In this study, we highlight the use of a simple self-assembly formation process that enables device miniaturization, and without the incorporation of intrinsically conductive nanostructures.

Polarization curves in Fig. 7b and c show a decrease in cell voltage when current flows due to overpotential, a characteristic behavior in fuel cells.[97] It is noteworthy that the polarization curve of the system with HEPES exhibits a dependency on ohmic loss, whereas the system with TPP is also influenced by mass transport loss. Several polarization curves were conducted without fuel or oxidant replenishment and without intermediate recharging steps. The dotted lines in Fig. 7b and c represent the polarization curves for the fifth measurement cycle. After these five discharge cycles, the EBFC with @TPP exhibits a 60% reduction in maximum power and a 24% decrease in OCV. In contrast, the EBFC with @HEP shows only a 45% reduction in maximum power and a decrease of less than 10% in OCV, while the changes in current density remain similar for both systems. Since the bioanode exhibits the same characteristics, these differences are likely associated with the stability of the biocathode. Consequently, the self-assembled structure formed by polyelectrolyte particles crosslinked with @HEP50,LIS is less affected during the EBFC discharge processes.

In terms of durability and stability, successive polarization curves provide insight into the changes observed in EBFCs constructed under specific conditions. While it is indeed possible to enhance the stability and longevity of these devices through tailored approaches, the present work aims to showcase the state of the art in biocathode optimization using a straightforward methodology. Just as the open-circuit voltage (OCV) can be improved through the use of DC–DC converters or serially connected EBFCs, long-term stability will depend on advances in enzyme engineering, the development of self-healing and mechanically robust matrices, or the integration of microfluidic systems.

4 Conclusions

For the design and optimization of the biocathode, crosslinking agents bearing phosphate and sulfonate groups were evaluated within the redox polyelectrolyte matrix. These species promote the formation of redox-active particles that enhance surface adsorption and facilitate electron transfer with the immobilized bacterial laccase. This effect was evidenced by increased catalytic current responses and improved j_c/j_0 ratios. Notably, these parameters were optimized through the incorporation of HEPES and TPP into the polyelectrolyte matrix under low and high ionic strength conditions, respectively. The resulting biocathodes enabled the operation of an O_2–glucose membraneless enzymatic biofuel cell (EBFC) under neutral pH and static conditions, yielding competitive values of power density and open-circuit voltage (OCV). The systems developed in this study offer a promising alternative for powering low-consumption devices,[95,96] as they can operate under mild conditions, require no nanostructured conductive materials or separators—thus reducing costs—and are amenable to miniaturization. Key challenges remain, improving long-term stability, optimizing current density and replacing osmium complexes.[22,98–100] They may be addressed through the addition of a protective layer, the

use of mutant laccases and novel redox polyelectrolytes featuring organic redox centers.

Author contributions

The manuscript was written through contributions of all authors. All authors have given approval of the final version of the manuscript.

Conflicts of interest

There are no conflicts to declare.

Data availability

The data supporting this article have been included as part of the SI. Supplementary information: DLS measurement; IR bands intensities and angles; current density plots for biocathodes, the bioanode and solution-phase system; AFM images; and IR spectra corresponding to amide I and amide II bands. See DOI: **https://doi.org/10.1039/d5ta05877e**.

Acknowledgements

A. K. thanks a scholarship of Universidad de Buenos Aires (Argentina). S. A. W., M. L. C., O. A., S. E. H., F. B. and L. L. C. O. are research staff of CONICET (Argentina). Universidad de Buenos Aires (UBACYT 20020220400015BA), ANPCyT (BID PICT 2021-00065), SICyT (Redes Federales de Alto Impacto, EX-2023-42139041 – APN-DDYGD#MCT), Royal Society of Chemistry (Research Development and Travel Grant, D23-4569855075) and Asociación Universitaria Iberoamericana de Postgrado (Movilidad Postdoctoral 2024) are acknowledged for financial support.

References

1 J. Lee, K. Y. Kim, Y. Kwon and D. Y. Khang, *Adv. Funct. Mater.*, 2023, 2309386.
2 Y. Qi, X. He, Z. Li, Q. Ma, M. Lu, H. Su, C. Li and Q. Xu, *J. Energy Storage*, 2025, **107**, 115014.
3 M. Luqman, S. Alqaed, F. A. Almehmadi, N. Shakeel, M. I. Ahamed, R. S. Alshareef, A. E. Elkhalifah and M. A. Alharthi, *J. Electroanal. Chem.*, 2024, **962**, 118265.
4 M. A. Abdelkareem, Q. Abbas, E. T. Sayed, N. Shehata, J. Parambath, A. H. Alami and A. Olabi, *Energy*, 2024, **299**, 131127.
5 J. Cai, F. Shen, J. Zhao and X. Xiao, *iScience*, 2024, **27**, 108998.
6 Y. Zhang, H. Wang, H. Lu, S. Li and Y. Zhang, *iScience*, 2021, **24**, 102716.
7 M. Khan and S. Inamuddin, *Sci. Rep.*, 2024, **14**, 1–16.
8 Z. Li, R. Wu, K. Chen, W. Gu, Y.-H. P. Zhang and Z. Zhu, *Biosens. Bioelectron.*, 2023, **223**, 115019.
9 A. A. Babadi, R. Fakhlaei, S. Rahmati, S. Wang and W. J. Basirun, *Electrochim. Acta*, 2024, **506**, 145054.
10 N. B. Duong, V. M. Truong, Y.-S. Li, C.-L. Wang and H. Yang, *Energy Fuels*, 2020, **34**, 10050–10058.
11 S. Cosnier, A. J. Gross, F. Giroud and M. Holzinger, *Curr. Opin. Electrochem.*, 2018, **12**, 148–155.
12 N. T. Garland, R. Kaveti and A. J. Bandodkar, *Adv. Mater.*, 2023, 2303197.
13 N. A. Karim and H. Yang, *Appl. Sci.*, 2021, **11**, 5197.
14 S. Fan, F. Sun, Z. Huang, Y. Hao, W. Zhang, Y. Zhang, H. Yu and J. Liu, *J. Solid State Electrochem.*, 2025, **29**, 3293–3303.
15 L. Wang, W. Zhu, J. Zhang and J.-J. Zhu, *Biosensors*, 2023, **13**, 175.
16 N. Mano and A. de Poulpiquet, *Chem. Rev.*, 2018, **118**, 2392–2468.
17 D. Majdecka, S. Draminska, D. Janusek, P. Krysinski and R. Bilewicz, *Biosens. Bioelectron.*, 2018, **102**, 383–388.
18 G. Janusz, A. Pawlik, U. Świderska Burek, J. Polak, J. Sulej, A. Jarosz-Wilkołazka and A. Paszczyński, *Int. J. Mol. Sci.*, 2020, **21**, 966.
19 R. Debnath and T. Saha, *Biocatal. Agric. Biotechnol.*, 2020, **26**, 101645.
20 L. Arregui, M. Ayala, X. Gómez-Gil, G. Gutiérrez-Soto, C. E. Hernández-Luna, M. H. de los Santos, L. Levin, A. Rojo-Domínguez, D. Romero-Martínez, M. C. N. Saparrat, M. A. Trujillo-Roldán and N. A. Valdez-Cruz, *Microb. Cell Fact.*, 2019, **18**, 200.
21 M. Zhang, X. Wang, W. Liu, X. Cui, Y. Wang, L. Fan, H. Cui, Y. Shen, H. Cui and L. Zhang, *ACS Appl. Mater. Interfaces*, 2025, **17**, 2355–2364.
22 X. Xiao, H. qi Xia, R. Wu, L. Bai, L. Yan, E. Magner, S. Cosnier, E. Lojou, Z. Zhu and A. Liu, *Chem. Rev.*, 2019, **119**, 9509–9558.
23 L. L. Coria-Oriundo, F. Battaglini and S. A. Wirth, *Ecotoxicol. Environ. Saf.*, 2021, **217**, 112237.
24 T. Ma, A. D. Easley, R. M. Thakur, K. T. Mohanty, C. Wang and J. L. Lutkenhaus, *Annu. Rev. Chem. Biomol. Eng.*, 2023, **14**, 187–216.
25 R. Suzuki, I. Shitanda, T. Aikawa, T. Tojo, T. Kondo, S. Tsujimura, M. Itagaki and M. Yuasa, *J. Power Sources*, 2020, **479**, 228807.
26 B. Olszewski and K. Stolarczyk, *Catalysts*, 2018, **8**, 414.
27 L. L. Coria-Oriundo, M. L. Cortez, O. Azzaroni and F. Battaglini, *Soft Matter*, 2021, **17**, 5240–5247.
28 L. L. Coria-Oriundo, M. L. Cortez, S. E. Herrera, O. Azzaroni and F. Battaglini, *Synth. Met.*, 2023, **294**, 117308.
29 D. Zappi, L. L. Coria-Oriundo, E. Piccinini, M. Gramajo, C. von Bilderling, L. I. Pietrasanta, O. Azzaroni and F. Battaglini, *Phys. Chem. Chem. Phys.*, 2019, **21**, 22947–22954.
30 A. L. Goff, M. Holzinger and S. Cosnier, *Cell. Mol. Life Sci.*, 2015, **72**, 941–952.
31 E. Apuzzo, M. Cathcarth, A. S. Picco, C. von Bilderling, O. Azzaroni, M. L. Agazzi and S. E. Herrera, *Biomacromolecules*, 2025, **26**, 1171–1183.
32 S. Fanaee and M. J. Filiaggi, *Mater. Lett.*, 2024, **366**, 136525.
33 I. Z. Abidin, E. J. Murphy, G. W. Fehrenbach, N. Gately and I. Major, *Carbohydr. Polym. Technol. Appl.*, 2024, **7**, 100480.
34 J. Zhou, Y. Wan, M. A. C. Stuart, M. Wang and J. Wang, *Biomacromolecules*, 2023, **24**, 5759–5768.

35 Z. A. Digby, M. Yang, S. Lteif and J. B. Schlenoff, *Macromolecules*, 2022, **55**, 978–988.
36 C. Vranckx, L. Lambricht, V. Préat, O. Cornu, C. Dupont-Gillain and A. vander Straeten, *Langmuir*, 2022, **38**, 5579–5589.
37 P. Pinyou, V. Blay, A. Kamkaew, K. Chansaenpak, S. Kampaengsri, M. Tongnark, I. Reesunthia, T. Khonru and J. Jakmunee, *ChemElectroChem*, 2022, **9**, e202101597.
38 P. Zhang and Z. G. Wang, *Macromolecules*, 2021, **54**, 10994–11007.
39 Y. M. Li, J. Yuan, H. Ren, C. Y. Ji, Y. Tao, Y. Wu, L. Y. Chou, Y. B. Zhang and L. Cheng, *J. Am. Chem. Soc.*, 2021, **143**, 15378–15390.
40 K. Lim, Y. S. Lee, O. Simoska, F. Dong, M. Sima, R. J. Stewart and S. D. Minteer, *ACS Appl. Mater. Interfaces*, 2021, **13**, 10942–10951.
41 M. Yang, Z. A. Digby and J. B. Schlenoff, *Macromolecules*, 2020, **53**, 5465–5474.
42 S. V. Kononova, E. V. Kruchinina, V. A. Petrova, Y. G. Baklagina, K. A. Romashkova, A. S. Orekhov and V. V. Klechkovskaya, *Cellulose*, 2018, **25**, 7239–7259.
43 W. A. Marmisollé, J. Irigoyen, D. Gregurec, S. Moya and O. Azzaroni, *Adv. Funct. Mater.*, 2015, **25**, 4144–4152.
44 M. M. Hossain, M. Rezki, I. Shalayel, A. Zebda and S. Tsujimura, *ACS Appl. Mater. Interfaces*, 2024, **16**, 44017.
45 L. Babel, S. Bonnet-Gómez and K. Fromm, *Chemistry*, 2020, **2**, 193–202.
46 K. A. Schug and W. Lindner, *Chem. Rev.*, 2005, **105**, 67–113.
47 R. A. Al-Horani and U. R. Desai, *Tetrahedron*, 2010, **66**, 2907–2918.
48 J.-C. M. Díaz-González, R. A. Escalona-Villalpando, L. G. Arriaga, S. D. Minteer and J. R. Casanova-Moreno, *Electrochim. Acta*, 2020, **337**, 135782.
49 C. Peng, J. Liu, Y. Xie and J. Zhou, *Phys. Chem. Chem. Phys.*, 2016, **18**, 9979–9989.
50 D. A. Buckingham, F. P. Dwyer, H. A. Goodwin and A. M. Sargeson, *Aust. J. Chem.*, 1964, **17**, 325–336.
51 F. Mao and A. Heller, Transition Metal Complexes with Bidentate Ligand Having an Imidazole Ring, WO2001036430, 2001.
52 E. M. Kober, J. V. Caspar, B. P. Sullivan and T. J. Meyer, *Inorg. Chem.*, 1988, **27**, 4587–4598.
53 M. M. Bradford, *Anal. Biochem.*, 1976, **72**, 248–254.
54 G. Priano, G. González, M. Günther and F. Battaglini, *Electroanalysis*, 2008, **20**, 91–97.
55 L. Maldonado, S. E. Herrera, F. J. Williams and M. Tagliazucchi, *J. Phys. Chem. C*, 2022, **126**, 9956–9964.
56 E. A. Weiss, G. K. Kaufman, J. K. Kriebel, Z. Li, R. Schalek and G. M. Whitesides, *Langmuir*, 2007, **23**, 9686–9694.
57 L. L. Coria-Oriundo, S. E. Herrera, L. P. M. D. Leo and F. Battaglini, *ACS Appl. Polym. Mater.*, 2022, **4**, 7759–7769.
58 J. Fu, H. M. Fares and J. B. Schlenoff, *Macromolecules*, 2017, **50**, 1066–1074.
59 J. B. Schlenoff, *J. Chem. Phys.*, 2018, **149**, 163314.
60 J. B. Schlenoff, M. Yang, Z. A. Digby and Q. Wang, *Macromolecules*, 2019, **52**, 9149–9159.
61 G. E. Fenoy, E. Piccinini, W. Knoll, W. A. Marmisollé and O. Azzaroni, *Anal. Chem.*, 2022, **94**, 13820–13828.
62 M. L. Agazzi, S. E. Herrera, M. L. Cortez, W. A. Marmisollé, M. Tagliazucchi and O. Azzaroni, *Chem.–Eur. J.*, 2020, **26**, 2456–2463.
63 S. E. Herrera, M. L. Agazzi, M. L. Cortez, W. A. Marmisollé, M. Tagliazucchi and O. Azzaroni, *ChemPhysChem*, 2019, **20**, 1044–1053.
64 M. L. Agazzi, S. E. Herrera, M. L. Cortez, W. A. Marmisollé, C. von Bilderling, L. I. Pietrasanta and O. Azzaroni, *Soft Matter*, 2019, **15**, 1640–1650.
65 G. Pérez-Mitta, W. A. Marmisollé, A. G. Albesa, M. E. Toimil-Molares, C. Trautmann and O. Azzaroni, *Small*, 2018, **14**, 1702131.
66 L. M. Araque, A. Infantes-Molina, E. Rodríguez-Castellón, Y. Garro-Linck, B. Franzoni, C. J. Pérez, G. J. Copello and J. M. Lázaro-Martínez, *Gels*, 2024, **10**, 790.
67 Y. Xu, J. Han, Y. Chai, S. Yuan, H. Lin and X. Zhang, *Mater. Sci. Eng., C*, 2018, **85**, 182–190.
68 M. Gierszewska and J. Ostrowska-Czubenko, *Prog. Chem. Appl. Chitin Its Deriv.*, 2016, **21**, 55–62.
69 J. D. Giraldo, V. H. Campos-Requena and B. L. Rivas, *Polym. Bull.*, 2019, **76**, 3879–3903.
70 T. E. Robinson, L. A. Arkinstall, S. C. Cox and L. M. Grover, *Comments Inorg. Chem.*, 2022, **42**, 47–59.
71 M. Mohana, P. T. Muthiah and R. J. Butcher, *Acta Crystallogr., Sect. C: Struct. Chem.*, 2017, **73**, 536–540.
72 I. Ahmad, A. A. Ganie and A. A. Dar, *CrystEngComm*, 2020, **22**, 3933–3942.
73 D. M. Mate and M. Alcalde, *Biotechnol. Adv.*, 2015, **33**, 25–40.
74 A. B. P. Lever, *Inorg. Chem.*, 1990, **29**, 1271–1285.
75 F. Mao and A. Heller, Transition Metal Complexes with (Pyridyl)imidazole Ligands, *US Pat.*, US7615637, 2009.
76 M. L. Cortez, A. L. Cukierman and F. Battaglini, *Electrochem. Commun.*, 2009, **11**, 990–993.
77 A. Barth, *Biochim. Biophys. Acta, Bioenerg.*, 2007, **1767**, 1073–1101.
78 T. Seki, K.-Y. Chiang, C.-C. Yu, X. Yu, M. Okuno, J. Hunger, Y. Nagata and M. Bonn, *J. Phys. Chem. Lett.*, 2020, **11**, 8459–8469.
79 J. Alvarez-Malmagro, M. Rueda and F. Prieto-Dapena, *Electrochim. Acta*, 2025, **530**, 146389.
80 J. Alvarez-Malmagro, L. Ruano, M. Cuartero-González, J. J. Nogueira and F. Prieto-Dapena, *J. Phys. Chem. B*, 2025, **129**, 4715–4727.
81 J. Alvarez-Malmagro, M. Rueda and F. Prieto-Dapena, *Electrochim. Acta*, 2023, **456**, 142465.
82 L. Shen, K. C. K. Cheng, M. Schroeder, P. Yang, E. N. G. Marsh, J. Lahann and Z. Chen, *Surf. Sci.*, 2016, **648**, 53–59.
83 M. Hoarau, S. Badieyan and E. N. G. Marsh, *Org. Biomol. Chem.*, 2017, **15**, 9539–9551.
84 S. ul Haque, N. Duteanu, S. Ciocan, A. Nasar and S. Inamuddin, *J. Environ. Manage.*, 2021, **298**, 113483.
85 H. Chen, T. Tang, C. A. Malapit, Y. S. Lee, M. B. Prater, N. S. Weliwatte and S. D. Minteer, *J. Am. Chem. Soc.*, 2022, **144**, 4047–4056.

86 S. Vanmathi, U. S. Jayapiriya, P. Sharma, O. P. Kulkarni and S. Goel, *Mater. Renew. Sustain. Energy*, 2025, **14**, 9.
87 P. S. Kumar, S. Vanmathi, H. Awasthi, I. Khan, R. K. Singh, V. K. Sharma, C. Pramanik and S. Goel, *Mater. Adv.*, 2024, **5**, 5932–5944.
88 J. Díaz-Sánchez, P. Roquero, M. Gimeno, O. Pilloni and L. Oropeza-Ramos, *Synth. Met.*, 2024, **307**, 117666.
89 S. Vanmathi and S. Goel, *J. Micromech. Microeng.*, 2024, **34**, 085004.
90 X. Wang and C. J. Kim, *Korean Chem. Eng. Res.*, 2022, **60**, 550–556.
91 J. Wan, L. Mi, Z. Tian, Q. Li and S. Liu, *J. Mater. Chem. B*, 2020, **8**, 3550–3556.
92 P. Bollella, G. Fusco, D. Stevar, L. Gorton, R. Ludwig, S. Ma, H. Boer, A. Koivula, C. Tortolini, G. Favero, R. Antiochia and F. Mazzei, *Sens. Actuators, B*, 2018, **256**, 921–930.
93 T. Kulkarni, D. Gupta and G. Slaughter, *2015 IEEE Sensors*, 2015, pp. 1–4.
94 F. Conzuelo, N. Marković, A. Ruff and W. Schuhmann, *Angew. Chem., Int. Ed.*, 2018, **57**, 13681–13685.
95 S. Alberti, E. Piccinini, P. G. Ramirez, G. S. Longo, M. Ceolín and O. Azzaroni, *Nanoscale*, 2021, **13**, 19098–19108.
96 J. Bai, D. Liu, X. Tian and S. Zhang, *J. Mater. Chem. C*, 2022, **10**, 13303–13311.
97 M. Rasmussen, S. Abdellaoui and S. D. Minteer, *Biosens. Bioelectron.*, 2016, **76**, 91–102.
98 L. C. I. Faria, S. Q. Nascimento, F. C. D. A. Lima, G. C. Sedenho, T. Bertaglia, R. M. Iost, J. C. P. de Souza, S. Lanceros-Méndez, S. D. Minteer, S. Cosnier, A. L. Furst and F. N. Crespilho, *ACS Energy Lett.*, 2025, 4470–4490.
99 L. Wang, X. Wu, B. S. Q. Su, R. Song, J.-R. Zhang and J.-J. Zhu, *Adv. Energy Sustainability Res.*, 2021, **2**, 2100031.
100 S. N. Jeyaraman and G. Slaughter, *Curr. Opin. Electrochem.*, 2021, **29**, 100753.

